J. Fluid Mech. (1970), *vol.* 41, *part* 1, *pp.* 47–80
Boeing Symposium on Turbulence

Wall-pressure fluctuations beneath turbulent boundary layers on a flat plate and a cylinder

By W. W. WILLMARTH AND C. S. YANG
Department of Aerospace Engineering, The University of Michigan

(Received 29 August 1969 and in revised form 24 November 1969)

Measurements of the turbulent pressure field on the outer surface of a 3 in. diameter cylinder aligned with the flow were made at a point approximately 24 ft. downstream of the origin of the turbulent boundary layer in an air stream of 145 ft./sec. The boundary-layer thickness was 2·78 in. and the Reynolds number based on momentum thickness was $2{\cdot}62 \times 10^4$. The wall-pressure measurements were made with pressure transducers constructed from 0·06 in. diameter lead–zirconate–titanate disks mounted flush with the wall. The measurements including root-mean-square, power spectrum, and correlations of the wall pressure are compared with the existing experimental results for the turbulent pressure field beneath a plane boundary layer. The streamwise convection speed deduced from longitudinal space-time correlation measurements was almost identical to that obtained in the plane boundary layer. The rate of decay of the maxima of the space-time correlation of the pressure produced by the convected eddies was double that in a plane boundary layer. The longitudinal and transverse scales of the pressure correlation were approximately equal (in a plane boundary layer the transverse scale is larger than longitudinal scale) and were one-half or less than the longitudinal scale in the plane boundary layer. It is concluded that the effect of the transverse curvature of the wall is an overall reduction in size of pressure-producing eddies. The reduction in transverse scale of the larger eddies is greater than that of the smaller eddies. In general, the smaller eddies decay more rapidly and produce greater spectral densities at high frequencies owing to the unchanged convection speed.

1. Introduction

This paper is concerned with the experimental measurement of wall-pressure fluctuations beneath a turbulent boundary layer on the outer surface of a cylinder aligned with a low-speed flow. The objective of the experiment is to determine the effect of transverse curvature on the wall-pressure fluctuations and on the structure of turbulence by comparison with measurements beneath flat plate boundary layers.

Knowledge of the pressure fluctuations beneath turbulent boundary layers is desired for numerous problems in fluid mechanics. The problems include: radiated sound produced by turbulence in the boundary layer when the surface is rigid, surface vibration and sound radiation produced when the turbulent

boundary layer is developed on a slightly flexible surface that is set in motion by the pressure fluctuations, and new knowledge of turbulence structure that can be obtained from wall-pressure measurements. In general, it has been observed that the wall-pressure fluctuations beneath a flat boundary layer are random, without periodic components and the root-mean-square wall pressure is of the order of 2·5 times the wall shear stress.

Using the method of space-time correlation, it was discovered (Willmarth 1958*a*) that the random pressure fluctuations were convected with a speed of approximately $0{\cdot}8U_\infty$. More detailed investigations (Willmarth & Woolridge 1962; Bull *et al.* 1963) have shown that the convection velocity varies with streamwise spatial separation of the measuring stations and that for small spatial separation the convection velocity is low, $0{\cdot}56U_\infty$ but increases to $0{\cdot}83U_\infty$ for very large spatial separation. The increase in convection velocity with streamwise separation of measuring points is attributed to the more rapid decay of the smaller pressure producing eddies.

Ideally, the effect of transverse curvature on wall-pressure fluctuations can be determined by comparing measurements made on a cylinder and on a flat plate at exactly the same Reynolds number, pressure gradient, Mach number and surface roughness. In actuality, measurements at low speeds have been made in the boundary layer on a smooth flat plate (Willmarth & Wooldridge 1962), at a slightly higher Reynolds number, based on momentum thickness, $R_\theta = 38{,}000$ than could be obtained on the cylinder, $R_\theta = 26{,}200$. On the other hand, we will also compare our measurements on the cylinder with the measurements of Bull *et al.* (1963), obtained beneath a flat plate boundary layer at slightly lower Reynolds number, $R_\theta = 19{,}500$.

Our knowledge of turbulent boundary layers with transverse curvature is not as extensive as it is for the flat plate boundary layer and is restricted to measurements and similarity laws for mean quantities only. The papers of Richmond (1957), Yu (1958), Yasuhara (1959), Reid & Wilson (1963) and Rao (1967) (these are discussed in §4) contain measurements and in some cases similarity laws for mean properties of turbulent boundary layers with varying amounts of transverse curvature.

It is often profitable in attempting to understand mean properties of the flow in a turbulent boundary layer to first consider the flow in a laminar boundary layer. Glauert & Lighthill (1955) have shown that the laminar boundary layer developed on a cylinder (when transverse curvature effects are large) has a much fuller profile than the Blasius boundary layer on a flat plate. In fact, the velocity near the wall is proportional to the logarithm of the distance from the cylinder axis and departs from that of the Blasius profile (in which u is linearly proportional to y near the wall) as the cylinder radius is reduced. The cause of this behaviour (as was clearly explained by Glauert & Lighthill) is that "the shearing force, on a cylinder of unit length, is equal to the shear stress $\mu\, du/dy$ multiplied by the circumference $2\pi(a+y)$ of the cylinder, and this force must be independent of y in the region where the acceleration of the fluid is negligible, that is, near the solid boundary".

One can expect that the presence of turbulence in a boundary layer with

transverse curvature will increase the rate of momentum exchange (just as it does in a flat plate boundary layer) with the result that, in comparison to the laminar boundary layer on a cylinder, the velocity profile will be fuller, the skin friction increased, and the stream-wise rate of growth of the boundary-layer thickness decreased.

The effect of transverse curvature on the structure of turbulence in the boundary layer and on the pressure fluctuations beneath it have not been studied. As a result of the present wall-pressure measurements, we have been able to qualitatively explain some of the effects of transverse curvature on turbulence structure.

2. Wind tunnel and cylindrical model

2.1. *Wind tunnel facility*

The experiments were carried out in the test section of the 5×7 ft. low-speed wind tunnel at the Gas Dynamics Laboratories, Department of Aerospace Engineering, The University of Michigan. The wind tunnel test section is 30 ft. long and is indoors. The settling chamber, fan and steel ducting that recirculates the air are out of doors. The total distance around the wind tunnel circuit is 332 ft. and the contraction ratio of the nozzle is 15 : 1.

The sound field in the tunnel test section has been measured by Willmarth & Wooldridge (1962). Wall-pressure correlation measurements on the floor of the test section showed a small peak at negative time delay which was caused by sound propagating upstream. From the measurements, it was determined that the sound energy amounted to approximately 1/20 of the energy in the turbulent wall-pressure fluctuations. In the present wall-pressure correlation measurements the sound energy is approximately 1/50 of the energy in turbulent wall-pressure fluctuations. The reduction of sound level was accomplished by better sealing against air leaks at the diffuser entrance and by reducing structural vibration in the downstream region of the test section and diffuser entrance.

The free-stream turbulence level measured by Tu & Willmarth (1966) at 200 ft./sec free stream speed was $\sqrt{(\overline{u}^2)}/U_\infty = 2{\cdot}50 \times 10^{-3}$ in the flow direction. The configuration of the wind tunnel has not been changed since that time.

2.2. *Cylindrical model*

A 40 ft. long, 3 in. diameter cylindrical model on which the boundary-layer measurements were made was installed along the centreline of the wind tunnel. It consisted of a 2 in. diameter steel tubing with $\frac{1}{8}$ in. wall thickness used as the 'backbone' of the model and a 3 in. steel tubing with 0·032 in. wall thickness used as the aerodynamic surface. The 3 in. tubing was positioned on the inner 2 in. tubing by means of adjustable set-screws. A 6 in. long ellipsoid of revolution and an 8 in. cone, both made of wood, were attached to the upstream and downstream end of the model respectively. The supports for the 2 in. tubing were so designed that they could furnish moments to reduce the mid-span deflexion of the tubing (figure 1). Upstream support consisted of five streamlined aircraft wires. Two wires, T_2, and one wire, T_1, produced a counter-clockwise moment. The other two wires at the bottom were dummy wires. The downstream support

was a unistrut frame with two unequal height columns (figure 2) which was covered with a streamlined fairing. When the 2 in. tubing was bolted on the columns, a clockwise moment was produced. The deflexion of the model in the

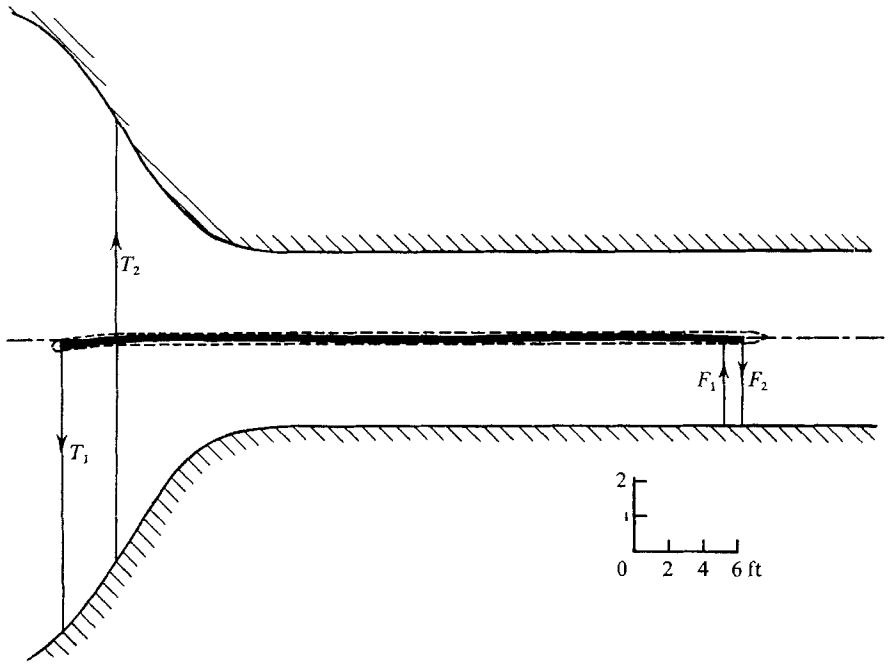

FIGURE 1. Schematic diagram of 2 in. diameter steel tubing installed in the wind tunnel as the backbone of the cylindrical model. ⁚⁚⁚, 3 in. diameter tubing; ▬, 2 in. diameter tubing.

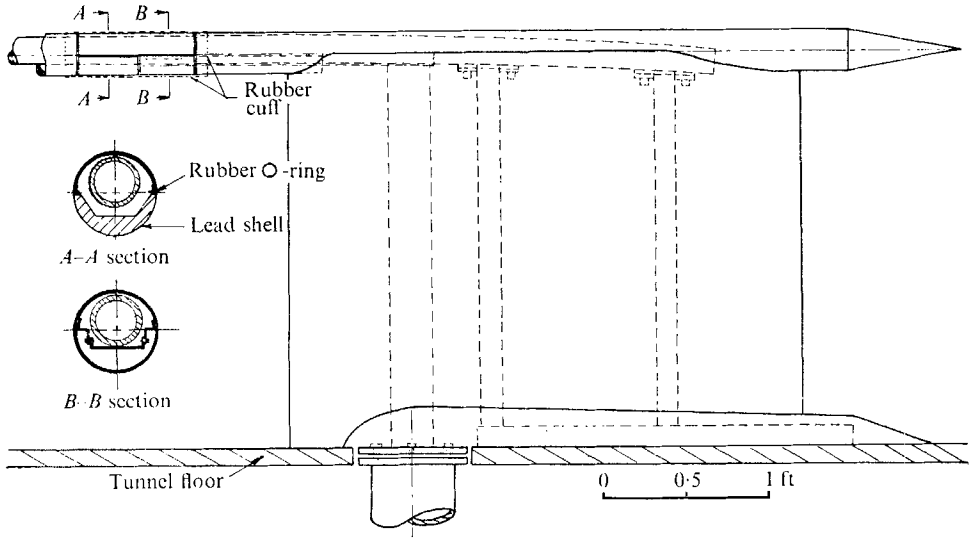

FIGURE 2. The test station and the rear support of the cylindrical model.

test section of the tunnel was reduced to a minimum value by properly adjusting the forces T_1 and F_2.

The wind velocity near the wire, T_1, was low, approximately $0{\cdot}09U_\infty$, therefore, the larger deflexion at the front end of the model did not effect the symmetry of the boundary-layer flow in the test section. The wind velocity near the wires, T_2, was approximately $0{\cdot}15U_\infty$. Since the terminals of the wires near the surface of the model were $\frac{1}{4}$ in. in diameter, they caused an asymmetry of the flow field around the cylinder in the test section. Four airfoil-shaped filets, made from balsa wood, were used to reduce the wake from the junction of the support wires and cylindrical surface with satisfactory results as described below.

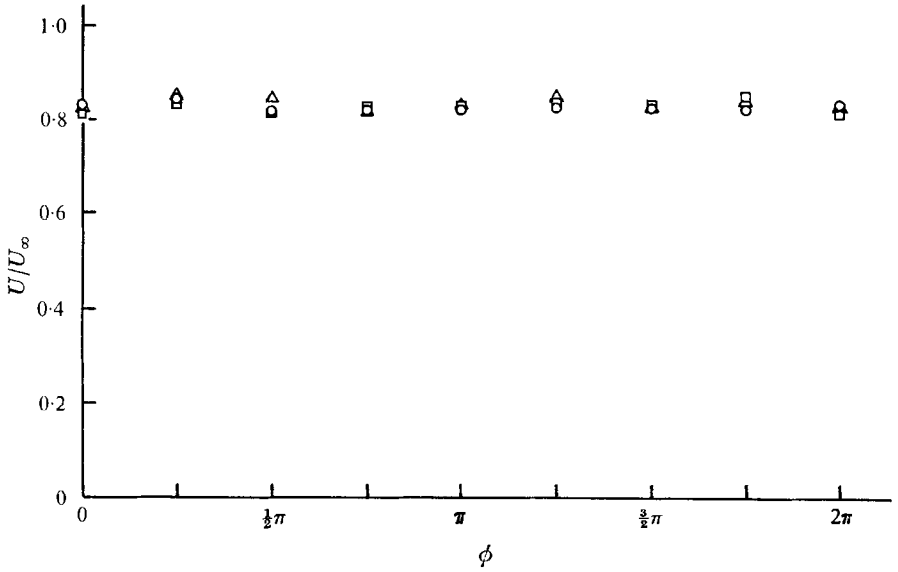

FIGURE 3. The symmetry of the velocity around the cylinder 0·65 in. from the wall at the transducer station. ○, U_∞ = 104 ft./sec; □, U_∞ = 138 ft./sec; △, U_∞ = 196 ft./sec. ϕ is azimuthal angle.

An impact pressure probe array which consisted of eight tubes 0·65 in. above the surface of the model equally spaced about the circumference of the cylinder was used to measure the circumferential velocity distribution at 16 and 24 ft. from the entrance of the test section. Initially the velocity distribution was very asymmetric with low velocity regions at four circumferential positions in the wake of the four upstream support wires. The use of balsa wood filets (see above) reduced the wake from the upstream wire supports and careful alignment of the model so that it was parallel to the stream by moving the downstream supporting struts reduced the asymmetry of the boundary layer to an acceptable level. The circumferential velocity distributions measured at the pressure transducer station (x = 24 ft.) for three different free stream velocities are plotted on figure 3, where ϕ is the azimuthal angle about the cylinder axis. The largest velocity deviation was $0{\cdot}02U_\infty$.

At its final position, the maximum vertical deflexion of the model in the test section of the tunnel was 0·39 in., and the maximum lateral deflexion was 0·25 in.

3. Instruments and experimental methods

3.1. *Instruments and methods for measuring mean properties of the flow*

To measure the velocity profile very near the surface of the cylinder a Pitot tube was installed on a traversing device. The Pitot tube was used in the Reynolds number range $50 < R = hU/\nu < 250$ where $h = 0{\cdot}003$ in. was the internal height of the mouth. The correction to the reading of the tube owing to viscous effects was negligible (see McMillan 1954). The maximum angle of attack of the Pitot tube which was mounted on a pivot in the traversing device was 10 degrees. It was experimentally confirmed that the angle of attack did not affect the total pressure reading up to an angle of 15 degrees (see Alexander, Baron & Comings 1953). The Pitot tube was moved on its pivot by the operator outside the test section, using a linkage and worm gear mechanism that was driven by a flexible shaft. The distance of the Pitot tube from the surface was measured with a cathetometer focused on the Pitot tube through the window of the tunnel.

The static pressure was measured with a slender tube parallel to the stream direction in contact with the surface of the cylinder. The tube was a long 0·065 in. diameter hypodermic tubing with one end sealed. A 0·035 in. diameter hole was drilled in the tube $3\frac{1}{2}$ in. from the sealed end.

The difference between Pitot and static pressure was measured with a precision single-tube manometer† with a resolution of 0·001 in. using water as the indicating liquid.

The velocity profiles quite far from the wall, $y/\delta > 0{\cdot}2$, were measured with a Pitot tube rake which consisted of 10 Pitot tubes and two static tubes at different heights from the wall.

The wall-shear stress was measured according to Preston's method (Preston 1954) using a 0·042 in. diameter Pitot tube in contact with the surface of the cylinder. The calibration given by Patel (1965) was used for calculation of wall-shear stress.

3.2. *Instruments and methods for measuring the turbulent pressure field*

At the test station, 24 ft. from the entrance of the test section, the lower half of the model was replaced by a $4\frac{1}{2}$ in. long, 3 in. diameter, semi-cylindrical lead shell (figure 2). There were 13 transducer elements, which were 0·06 in. diameter and 0·020 in. thick lead–zirconate–titanate (PZT-5) disks mounted permanently flush with the outer surface of the lead shell. The arrangement of the transducers which was selected to efficiently obtain the spatial correlation of the pressure field is shown in figure 4.

Figure 5(*a*) shows the cross-section of a single transducer plug mounted in the lead shell. A fine copper wire (0·002 in. diameter) was attached to the front surface of the phenolic plug and brought out through the hole in it which was then filled with wax. The PZT-5 disk was glued on the plug with conducting cement.‡ This plug was then inserted into a 0·063 in. diameter hole drilled through the lead shell. The position of the plug was so adjusted that the PZT-5 disk was flush

† The Meriam Instrument Co., Micro-Manometer Model 34 FB 2.

‡ SC 12 MicroCircuits Co., New Buffalo, Michigan.

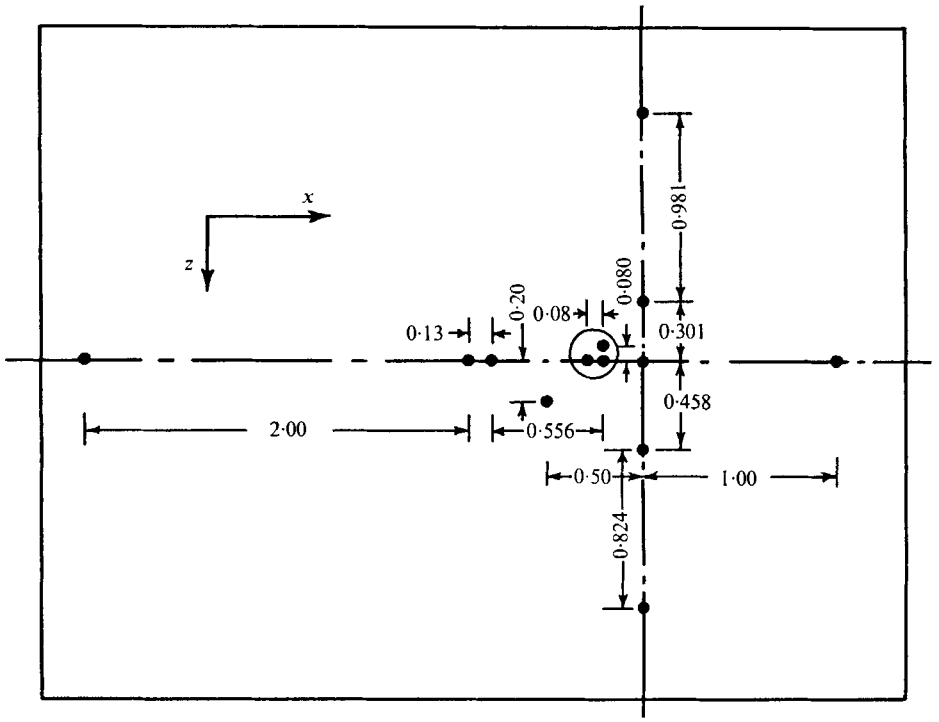

FIGURE 4. Developed view of the spatial arrangement of the pressure transducers; $z = a\phi$.

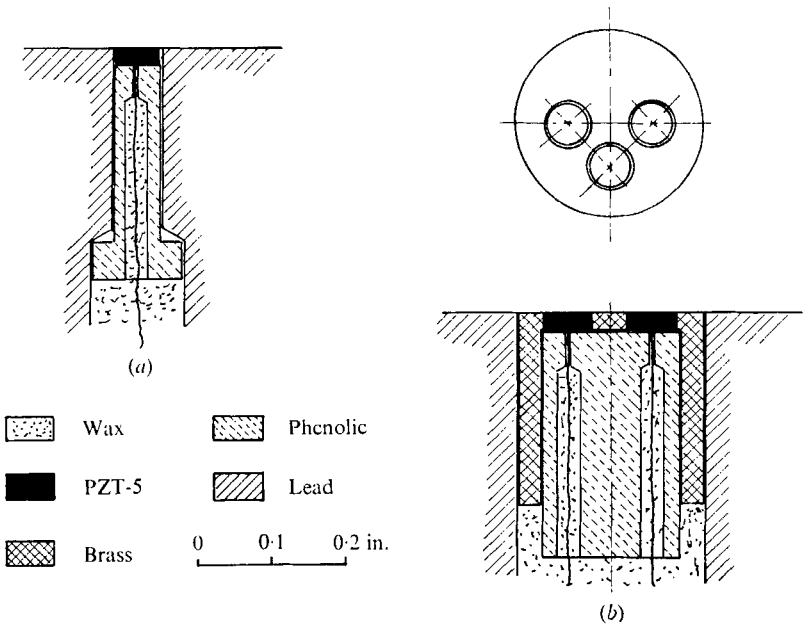

FIGURE 5. Pressure transducers assembly. (*a*) Single transducer plug; (*b*) triple transducer plug.

with the lead surface. The remainder of the hole was filled with vacuum sealing wax, a product of Central Scientific Company. On the front surface, the transducer was electrically connected to the lead shell with a thin coat of conducting silver paint.†

The cross-section of the triple transducer plug is shown on figure 5(*b*). The construction differed from the single transducer plug in that an additional brass sleeve was used and the method of ground connexion was altered. The outer surface of the brass sleeve was curved to match the surface curvature of the lead shell. The electrical connexion between the brass and the PZT-5 disks was provided by gluing a piece of aluminized mylar plastic sheet (0·0005 in. thick) on the surface. The brass sleeve was in contact with lead.

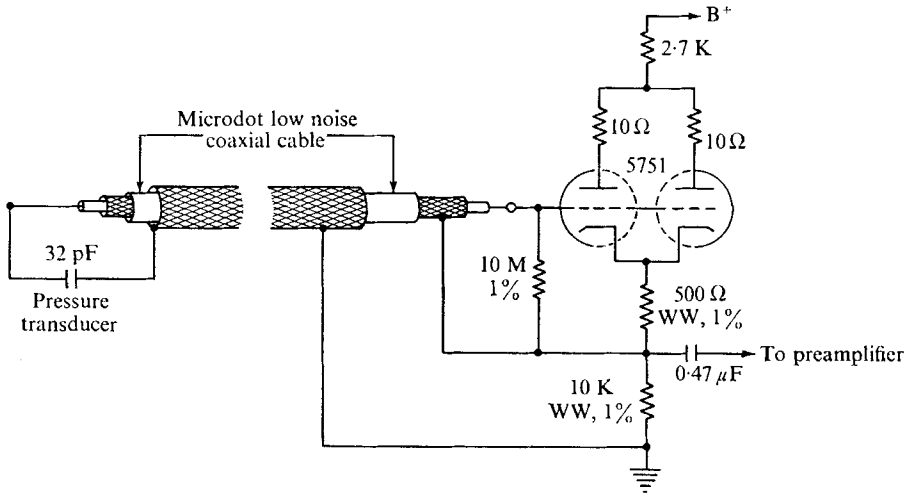

FIGURE 6. Circuit diagram for pressure transducers and cathode follower.

Thirteen short Microdot coaxial cables with Microdot connectors at one end were glued on the inner surface of the lead shell with epoxy cement.‡ The copper wires at the back of the transducer plugs were soldered to the central conductor of the cables. Two 7 ft. long Microdot coaxial cables with additional outer shielding to make a tri-axial cable were used to conduct the transducer signals to the input of the cathode followers and preamplifiers. To reduce parasitic capacitance of the long cable, the coaxial cable shield was driven by a voltage proportional to the transducer signal and the additional outer shield outside the cable was used as ground (figure 6). The capacitance of the pressure transducer was 32 pF. The use of a driven shield effectively reduced the capacity of the long cables leading to the cathode followers to a low value.

In order to seal the air gap between the lead shell and the steel tubing, and to support the lead shell it was held on the model by a thin rubber cuff (0·008 in. thick). The outer surface of the 3 in. diameter steel tubing above the lead shell was attached to a vibration isolated structure beneath the 2 in. diameter pipe and running to the rear and down to a massive structure mounted on rubber

† SC12 MicroCircuits Co., New Buffalo, Michigan.

‡ Epo-lux, Steelcote Mfg. Co., no 185A.

pads beneath the tunnel, see figure 2. Thus, the major portion of the cylinder beneath the rubber cuff was not in contact with the wind tunnel wall or cylinder. This was essential to reduce the signals produced by vibration of the transducers to a low level. With this mounting no corrections for vibration were necessary. Four rubber O-rings were placed between the contact surfaces of the lead and the steel to further isolate the lead shell and transducers from vibration.

The frequency response of the transducers was assumed to be flat over the frequency range of interest, $f \leqslant 50{,}000$ Hz. Willmarth (1958*b*) has shown, by shock tube calibration, that transducers larger than the present transducers which were made in similar manner had a flat frequency response up to at least 50,000 Hz. The absolute calibration of the pressure transducers was carried out 'in situ' beneath the rubber cuff with the lead shell installed on the cylindrical model. A prevously calibrated transducer (Willmarth & Wooldridge 1962) and the new pressure transducers were enclosed inside a Helmholtz resonator which was made from a narrow mouthed bottle whose bottom was cut to fit the cylinder. The joint was sealed with clay and the Helmholtz resonator was excited at 250 Hz by a carefully positioned low speed air jet blowing across the bottle mouth. The calibration was obtained by comparing the output of the two transducers inside the Helmholtz resonator. The sensitivity of the transducers was typically $1{\cdot}32 \times 10^{-6}$ V/dyne/cm^2.

The transducers were connected to a cathode follower with high input impedence of $1{\cdot}2 \times 10^8$ ohms (figure 6) followed by a low noise preamplifier and amplifier system with a maximum gain of 10^5 (see Willmarth & Wooldridge 1962). The band width of the amplifier was adjustable between 1 Hz and 160 KHz. The electrical signals from the pressure transducers were recorded on a three-channel Ampex FR 1100 tape recorder which had a band width from d.c. to 20 KHz. The root-mean-square wall pressure was measured with a Ballantine model 320 true r.m.s. meter.

The spectrum of the fluctuating wall pressure was obtained by passing the signal through a Tektronix Type 1L5 spectrum analyzer plug-in unit† which was driven by a Tektronix Type 544 oscilloscope. The output was recorded on a Hewlett Packard Model 2DR-2M x–y recorder.

The correlations of the wall pressure were measured with a Princeton Applied Research Model 101 correlation function computer whose output was recorded with the above x–y recorder. Two Kron-Hite Model 310-AB variable band pass filters were used for correlation measurements in narrow frequency bands.

4. Mean flow field

4.1. *Equations of motion*

Using the usual boundary-layer approximations, the boundary-layer equations for the mean motion written in cylindrical co-ordinates with the x-axis parallel to the stream, are

$$U\frac{\partial U}{\partial x}+V\frac{\partial U}{\partial r}=-\frac{1}{\rho}\frac{\partial P}{\partial x}+\frac{\nu}{r}\frac{\partial}{\partial r}\left(r\frac{\partial U}{\partial r}\right)-\frac{1}{r}\frac{\partial}{\partial r}(r\overline{uv}) \tag{1}$$

† The unit was calibrated in amplitude and frequency before use.

and
$$\partial P/\partial r = 0, \tag{2}$$

with continuity equation
$$\frac{\partial U}{\partial x} + \frac{1}{r}\frac{\partial (rV)}{\partial r} = 0, \tag{3}$$

where U and V are the mean velocity components parallel and normal to the stream. P is the mean pressure and u and v are the fluctuating velocity components parallel and normal to the stream.

The displacement thickness, δ^*, and the momentum thickness, θ, for a fluid of constant density are defined by

$$(\delta^* + a)^2 - a^2 = \int_{a^2}^{(\delta+a)^2} \left(1 - \frac{U}{U_\infty}\right) dr^2 \tag{4}$$

and
$$(\theta + a)^2 - a^2 = \int_{a^2}^{(\delta+a)^2} \left(1 - \frac{U}{U_\infty}\right)\frac{U}{U_\infty}\, dr^2 \tag{5}$$

(see Moore 1952). Here a is the cylinder radius.

4.2. *Similarity laws*

The correct similarity laws for the mean flow in an axially symmetric boundary layer with zero-pressure gradient have not yet been firmly established. If the amount of transverse curvature is not too large, the most logical approach might be to assume that the usual law of the wall and law of the wake are still valid. However, one must recognize immediately that in this problem there is an additional dimensional length parameter, a, the radius of curvature of the wall. Thus, in the wall region dimensional considerations indicate a functional relationship

$$\frac{U}{U_\tau} = F\left(\frac{yU_\tau}{\nu}, \frac{aU_\tau}{\nu}\right) \tag{6}$$

and in the wake region,
$$\frac{U_\infty - U}{U_\tau} = G\left(\frac{y}{\delta}, \frac{\delta}{a}\right). \tag{7}$$

Here, we have made all the usual assumptions about the mean flow in the wall and wake region (see Clauser 1956, p. 1), and have simply added the additional length, a, the transverse radius of curvature of the wall.

It is quite possible that the traditional division of mean flow properties into a wall region and wake region may not be valid when the transverse curvature is large, $\delta/a \gg 1$. One may visualize a very small radius of curvature of the wall in which the region occupied by fluid motions obeying the law of the wall (which is assumed to be of the form of equation (6)) is a very small fraction of the region occupied by the turbulent boundary-layer flow. In other words, the boundary layer on a slender rod ($a/\delta \to 0$) is almost all a wake-like flow and the region near the wall (which, if it is called the wall region, must be independent of free stream conditions) would be a very small region containing the viscous sublayer. It is possible that in the limit $a \to 0$ the wall region contains only the viscous sublayer.

In our present work we have been restricted to boundary layers in which $\delta/a \approx 2$. For this case we will assume that the traditional (but modified, see equations (6) and (7)) division of the mean flow into a wall region and a wake region is valid. In addition, we will also adopt the procedure of Richmond

(1957), for the flow in the region near the wall. Essentially what Richmond did (under Coles' guidance) was to assume that there was a region near the wall where the mean flow was dominated by the wall. He then obtained a law of the wall for the axisymmetric boundary layer using Coles' streamline hypothesis in that region. Coles' streamline hypothesis (Coles 1955, p. 153) (which is true in the region near the wall of a two-dimensional turbulent boundary layer) asserts that U/U_τ is constant on mean streamlines where $U_\tau = \sqrt{(\tau_w/\rho)}$ and τ_w is the wall-shear stress. Therefore, we can expect Richmond's procedure for the wall region of the axisymmetric boundary layer to be valid in the region near the wall where the turbulent flow is still essentially two-dimensional (or, in other words, when the ratio y/a is small). If y/a is not small, the similarity law obtained from the streamline hypothesis may be incorrect.

We will give for reference (since Richmond's paper is not readily available) a brief description of his procedure for obtaining the similarity law. He assumes (the streamline hypothesis) that U/U_τ is constant on the mean streamlines. Therefore, using the stream function, ψ,

$$\frac{U}{U_\tau} = \phi(C\psi); \tag{8}$$

inverting this expression

$$\psi = \frac{1}{C} H\left(\frac{U}{U_\tau}\right). \tag{9}$$

The continuity equation (see (3)) defines the stream function

$$Ur = \frac{\partial \psi}{\partial r}; \quad Vr = -\frac{\partial \psi}{\partial x}. \tag{10}$$

Thus, from (9) and (10)

$$U_\tau = \frac{1}{UrC} H'\left(\frac{U}{U_\tau}\right)\frac{\partial U}{\partial r}. \tag{11}$$

Integrating U_τ over the area between the wall and radius r

$$\tfrac{1}{2}CU_\tau(r^2 - a^2) = G\left(\frac{U}{U_\tau}\right). \tag{12}$$

Inverting this expression, we obtain

$$\frac{U}{U_\tau} = F[\tfrac{1}{2}CU_\tau(r^2 - a^2)]. \tag{13}$$

The constant C is evaluated at the wall (assume $F'(0) = 1$), and $C = 1/\nu a$. Richmond's law of the wall is

$$\frac{U}{U_\tau} = F\left[\frac{yU_\tau}{\nu}\left(1 + \frac{y}{2a}\right)\right]. \tag{14}$$

Using the new co-ordinate $(U_\tau y/\nu)(1 + y/2a)$, one can write the law of the wall in the form

$$\frac{U}{U_\tau} = 5{\cdot}75 \log_{10}\left[\frac{U_\tau y}{\nu}\left(1 + \frac{y}{2a}\right)\right] + 5{\cdot}10, \tag{15}$$

where the function F is the usual (empirically verified) form for two-dimensional flow outside the sublayer. It appears that the above equation (14) provides an

adequate representation of our results for $\delta/a \approx 2$. There are indications from Richmond's (1957) work, that the region of validity of (14) becomes a rather small region near the wall as δ/a becomes large.

There are a number of other investigations of the mean flow field in the region near the wall. In the work of Yu (1958) (which includes experimental results) a different method was developed (at Iowa Institute of Hydraulic Research under the guidance of Rouse and Landweber) for correlation of the mean flow in the wall region and the wake region. In Yu's formulation, the wall region contains the free-stream velocity as an additional parameter (in addition to the parameters ν, U_τ and a). We have chosen Richmond's method for data presentation because in the wall region one should not have free-stream velocity as a parameter.

Yasuhara (1959) has reported mean velocity measurements on a slender cylinder for cases in which $\delta/a \approx 1$. Yasuhara presented his results in the form advocated by Richmond (1957), with results quite similar to Richmond's and to our present measurements.

Rao (1967) has reported a different form for the law of the wall. His form is derived on the basis that for a slender cylinder, $\delta/a \gg 1$, the sublayer thickness is comparable to the radius of transverse curvature. His reasoning suggests that

$$\frac{U}{U_\tau} = \frac{U_\tau a}{\nu} \ln \frac{r}{a}. \tag{16}$$

This form is certainly correct in the region very near the wall where $U = V = u = v = 0$ (see (1)). We doubt that, as suggested by Rao (1967), (16) can be valid in a region extending from the wall as far as the radius of curvature of the cylinder when $\delta/a \gg 1$. Thus, we believe that the correct conception of the sublayer is a region dominated by wall effects and that no matter how large the ratio δ/a becomes the sublayer thickness is always small compared to the radius of curvature of the surface, a. If this were not true, the turbulent eddying flow would wash the fluid in the sublayer completely off the cylinder. Rao also proposes that throughout the boundary layer, for $\delta/a \gg 1$, the form of the velocity profile should be

$$\frac{U}{U_\tau} = F\left(\frac{U_\tau a}{\nu} \ln \frac{r}{a}\right), \tag{17}$$

where F is the function obtained for the law of the wall in a two-dimensional flow. We have not used this form, (17), because it has the obvious property (since the function F is a logarithm in the wall region) of taking the logarithm of the logarithm of r/a. This reduces scatter of data points for large r and it requires extremely accurate measurements to determine the validity of the formulation, (17). It would appear that the mean flow field in a turbulent boundary layer with transverse curvature is not well understood when δ/a is large. It appears that the law of the wall, (14), and (16) have only a small region of validity when $\delta/a \gg 1$ (see Richmond 1957). Also, an appropriate similarity law for the wake region has not been firmly established for large or small values of δ/a.

4.3. *Experimental results for mean flow field*

The streamwise static pressure distribution along the surface of the cylinder at two different free-stream velocities was measured as described in §3.1. The results were plotted in figure 7, showing a slight streamwise pressure increase. This was caused by the too rapid divergence of the side walls of the wind-tunnel test section. The mean flow field in the flat plate (two-dimensional) boundary layer on the floor of the test section has been investigated by Willmarth & Wooldridge (1962). It was found that in the pressure gradient of figure 7, the mean velocity profiles were (within the accuracy of the measurements) those generally accepted for an equilibrium two-dimensional boundary layer (see Coles 1954). In addition, the dimensionless shape factor, Γ, of Buri (see Schlichting 1968, p. 629) was $\Gamma \approx -6 \times 10^{-4}$ or approximately 1/100 of the value, $\Gamma = -7 \times 10^{-2}$, required for separation of a two-dimensional turbulent boundary layer. We can conclude that the slight adverse pressure gradient $\partial C_p/\partial x = 3 \times 10^{-3}$ ft.$^{-1}$, will not cause the mean flow in the boundary layer to deviate appreciably from the zero pressure gradient case.

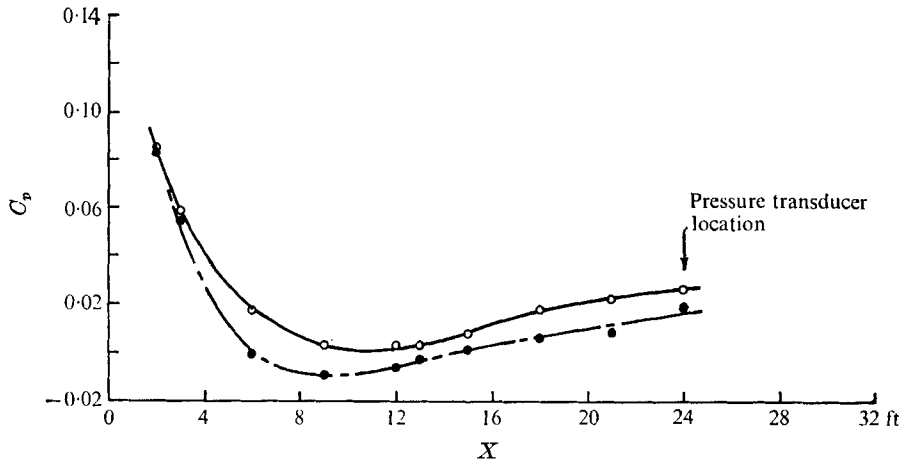

FIGURE 7. Pressure gradient along the cylinder. ○, $U_\infty = 99$ ft./sec; ●, $U_\infty = 199$ ft./sec.

The wall shear stress was measured using a Preston tube as described in §3.1. The results are displayed in figure 8 (see also tables 1 and 2) along with the measurements of Richmond (1957), Yasuhara (1959) and Yu (1958)† for axially symmetric turbulent boundary layers with approximately the same ratio of θ/a as our experiments. The present measurements agree reasonably well with previous results at $R_\theta \approx 10^4$ and extend the skin friction measurements to $R_\theta \approx 3{\cdot}5 \times 10^4$ for $0{\cdot}15 < \theta/a < 0{\cdot}25$. Note that the skin friction coefficient is appreciably larger than in a flat plate turbulent boundary layer.

The velocity profiles measured at the location of the pressure transducers are plotted in figure 9 in the form suggested by (14). The results of the velocity

† Yu's (1958) definition of θ is different from ours (equation (5)). When θ is calculated according to (5), Yu's value of R_θ is reduced by approximately 15 %.

profile measurements (figure 9) show that Richmond's modified law of the wall (equation (14)) agrees fairly well with measurements of the present investigation for $\delta/a \leqslant 2$. In table 2 are summarized the various mean properties of turbulent boundary layers with transverse curvature that have been measured in this investigation.

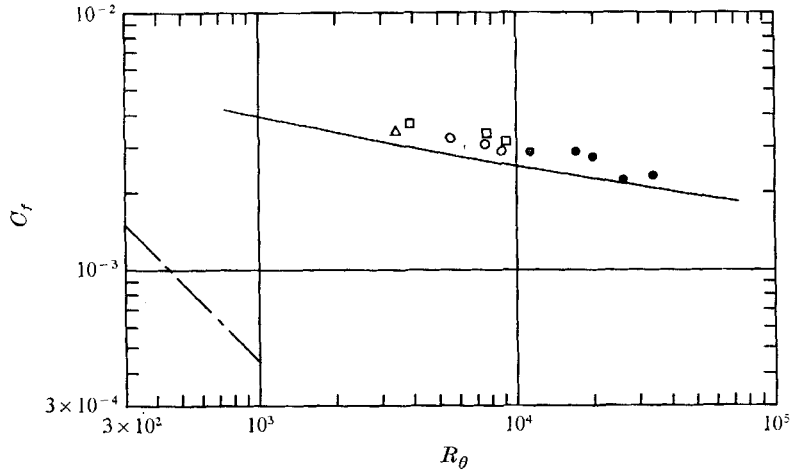

FIGURE 8. Skin friction coefficient. △, Yasuhara, $\theta/a = 0{\cdot}154$; □, Yu, $0{\cdot}20 < \theta/a < 0{\cdot}25$; ○, Richmond, $0{\cdot}14 < \theta/a < 0{\cdot}21$; ●, present, $0{\cdot}15 < \theta/a < 0{\cdot}25$; – – –, Blasius; ——, Coles' flat plate.

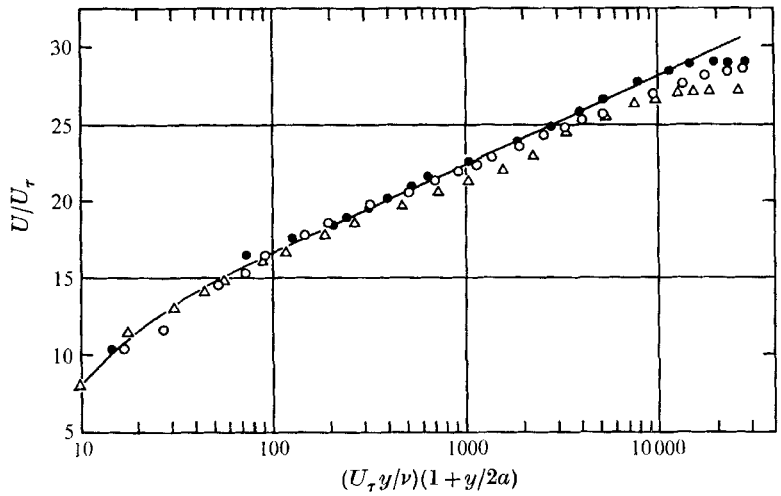

FIGURE 9. Mean velocity profiles in the axially symmetric turbulent boundary layer. ○, $U_\infty = 200$ ft./sec; ●, $U_\infty = 145$ ft./sec; △, $U_\infty = 100$ ft./sec; ——, Coles' ideal turbulent boundary layer according to equation (14).

5. Experimental results

The measurements of the wall-pressure fluctuations beneath the axially symmetric boundary layer will be discussed in the light of our knowledge of wall-pressure fluctuations beneath a plane two-dimensional boundary layer. The

X(ft.)	U_∞(ft./sec)	θ(in.)	θ/a	R_θ	C_f	Source
8	30	0·253	0·253	3860	0·0037	Yu (1958)
8	60	0·247	0·247	7600	0·00338	
7	90	0·20	0·200	9010	0·00315	
8	154	0·069	0·138	5540	0·00323	Richmond (1957)
9	154	0·094	0·188	7540	0·00305	
10	154	0·109	0·210	8750	0·00290	
3·28	110	0·051	0·154	3360	0·00347	Yasuhara (1959)

X = Distance from the nose of the cylindrical model.

TABLE 1. Summary of results of skin friction measurements for turbulent boundary layers with transverse curvature

X(ft.)	U_∞ (ft./sec)	R_a	θ(in.)	θ/a	U_τ	C_f	C_f/C_f'	R_θ	$\delta/2a$	δ^*/θ
24	200	134,000	0·382	0·254	6·96	0·00230	1·11	33,800	1·007	1·15
24	145	115,000	0·341	0·228	4·98	0·00219	1·02	26,200	0·926	1·23
24	100	70,200	0·359	0·238	3·83	0·00276	1·22	16,800	1·073	1·14
16	198	136,000	0·218	0·146	7·30	0·00258	1·14	19,800	0·607	1·14
16	101	69,800	0·244	0·162	3·92	0·00284	1·14	11,300	0·80	1·21

C_f' (flat plate) due to Coles (1954).

TABLE 2. Mean properties of the axially symmetric turbulent boundary measured in the present investigation

most striking property of the wall-pressure fluctuations beneath a plane-boundary layer is the now well-known fact that the random pressure fluctuations are convected at speeds of the order of $0{\cdot}5U_\infty$ to $0{\cdot}85U_\infty$. In the present experiment we have found that the space-time correlation of wall-pressure fluctuations beneath the boundary layer with transverse curvature also shows convection and decay, but with the important difference that the rate of decay of pressure correlations is more rapid. This will be discussed in detail below along with other statistical measurements of the random pressure field which include the mean-square; power spectrum; lateral, oblique, and longitudinal correlations (with zero time delay); and narrow frequency band correlations of the wall-pressure fluctuations.

5.1. *Longitudinal space-time correlations of the wall pressure*

The normalized wall-pressure correlation is

$$R_{pp}(x_1, x_3, \tau) = \frac{\overline{p(x, z, t)\, p(x + x_1, z + x_3, t + \tau)}}{\sqrt{[\overline{p^2(x, z, t)}\, \overline{p^2(x + x_1, z + x_3, t + \tau)}]}}, \tag{18}$$

where the over-bar denotes a time average and the co-ordinate z (and x_3) lies in the surface of the cylinder and is normal to the axis (and the free stream). The results of our longitudinal space-time pressure correlation measurements in the frequency band $0{\cdot}144 < \omega\delta^*/U_\infty < 28{\cdot}8$ are shown in figure 10. The correlation curves (reading from top to bottom) were measured at increasing

values of spatial separation. The peaks of the correlation occur at larger and larger time delay as the spatial separation increases (note that the displaced time origins are indicated by small vertical bars on figure 10).† At large spatial separations a small peak appeared on the left branch of the curve, $\tau < 0$. The peak is caused by upstream propagation of pressure fluctuations owing to the sound produced in the wind-tunnel diffuser and fan. The mean-square sound pressure in the test section can be estimated from the average maximum value of the peak on the space-time correlation curves for $\tau < 0$. It is approximately

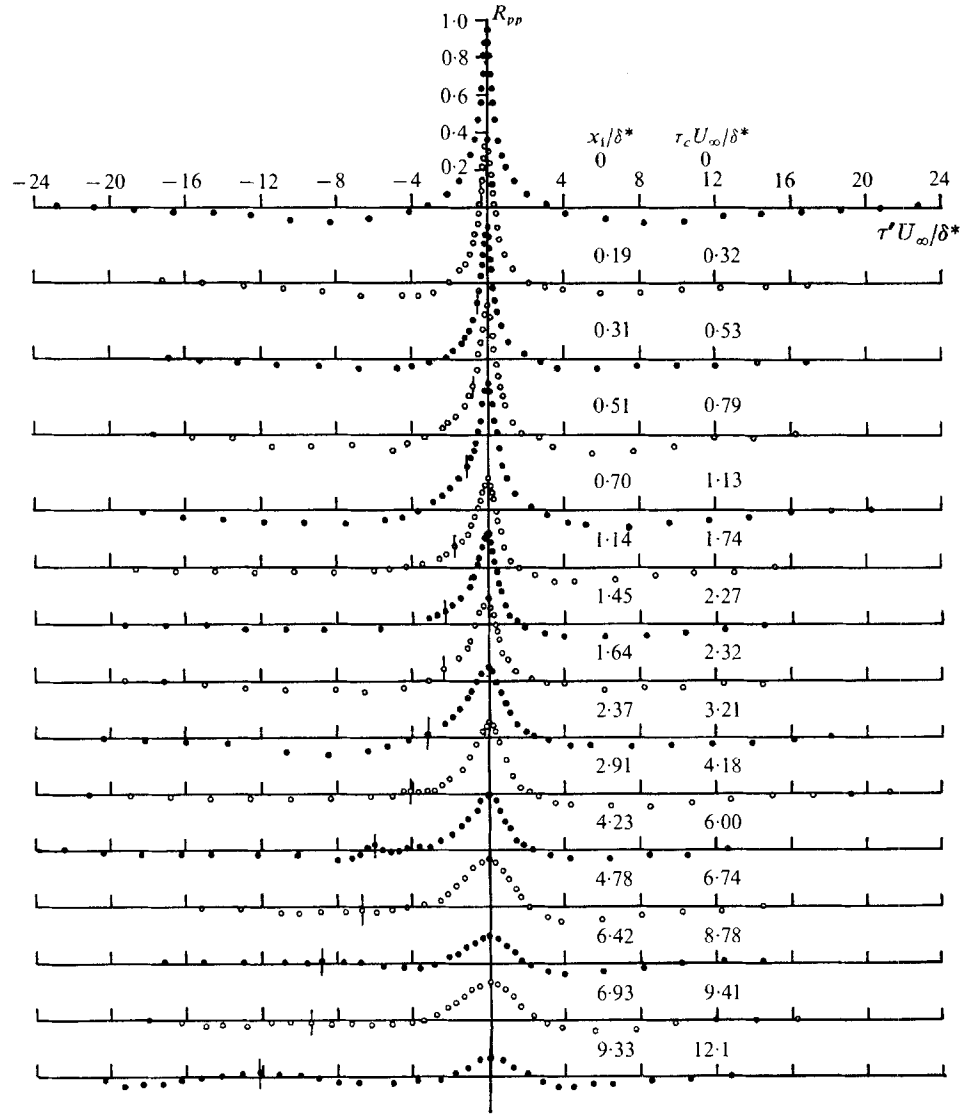

FIGURE 10. Longitudinal space-time correlation of wall pressure, $x_3 = 0$.

† In figure 10 the time delay $\tau = \tau_c + \tau'$, where τ_c is the time delay for maximum R_{pp} at constant x_1 and x_3.

$0{\cdot}02\overline{p^2}$. This value was used in estimating the true value of the spatial correlations of wall pressure (see appendix A).

In the present investigation, the convection speed is identical (within the experimental error) with the convection speed in a plane boundary layer. Figure 11 shows the location, for various streamwise spatial separations and time delays,

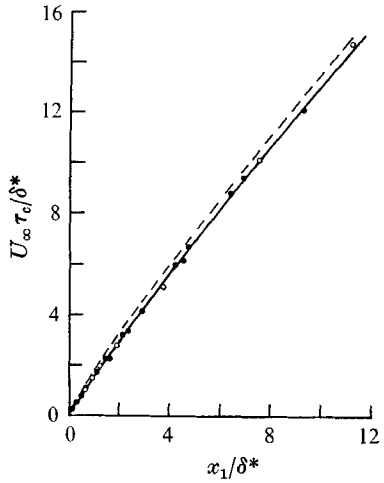

FIGURE 11. Time delay for R_{pp} maximum at various constant values of x_1, $x_3 = 0$. ●, $\delta/a = 2$; ○, $\delta/a = 0$, Willmarth & Wooldridge; – – –, $\delta/a = 0$, Bull.

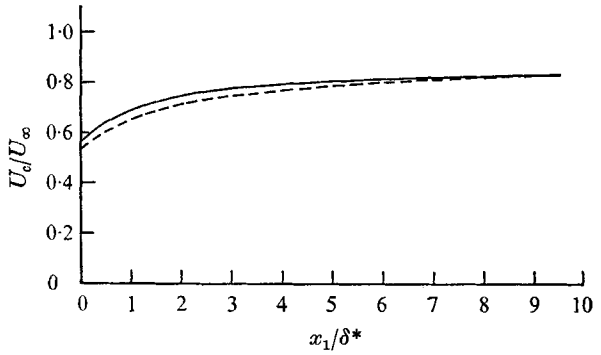

FIGURE 12. Local convection speed of the pressure-producing turbulent eddies. ——, $\delta/a = 2$ and $\delta/a = 0$, Willmarth & Wooldridge; – – –, $\delta/a = 0$, Bull.

of the maxima of the pressure correlation along with the two-dimensional results from Willmarth & Wooldridge (1962) and Bull *et al.* (1963). Figure 12 shows the convection speed for increasing values of spatial separation. The convection speed of figure 12 is obtained graphically from the slope of the locus of the peaks of pressure correlation of figure 11. The reader should note that this definition of convection speed is somewhat ambiguous since the correlation of the pressure decays in time and space. A perfectly definite convection speed is easy to define and to understand if one has a frozen random pattern convected at constant speed because the lines of constant correlation (the convection path) in the x_1,

τ plane will be parallel straight lines whose slope is the convection velocity. In the case of a decaying random field in which turbulence of various scales moving at different convection speeds is present, the reader is referred to a paper by Wills (1964) who has discussed the difficulties with the various definitions of convection speed and has proposed a convection speed definition based on maximizing the integral time scale. In practice, for our experiments, it is an almost impossible procedure to use Wills' definition of convection speed since one must measure pressure correlations while varying the spatial separation between the pressure transducers.† The surface curvature and the inaccessibility of the cylindrical model (in the centre of the tunnel) make this impractical. Also, it is not really necessary to use a precise definition of convection velocity because we are looking for changes from the convection properties of the two-dimensional wall-pressure fluctuation field. The definition of convection velocity used for the present work is precisely the same as that used in the previous plane boundary-layer experiments.

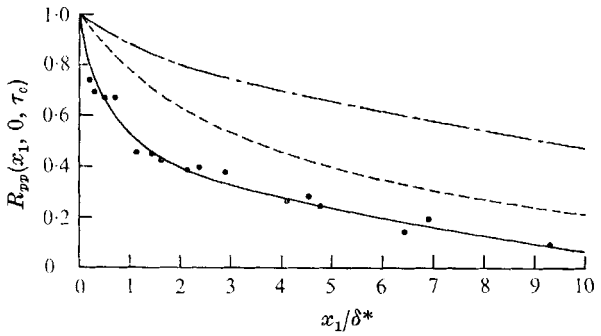

FIGURE 13. Decay of maximum wall-pressure correlation. ●, $\delta/a = 2$ peak values of figure 10; ——, plane boundary layer, Willmarth & Wooldridge; — — —, plane-boundary layer, Bull.

As we have already mentioned, the convection velocity is the same as that found beneath a plane boundary layer. The measurements show in each case an increase in convection velocity from approximately $0{\cdot}56U_\infty$ to $0{\cdot}83U_\infty$ as the longitudinal spatial separation is increased. The increase in convection velocity is caused by the more rapid decay of the smaller pressure producing eddies near the wall. After the smaller eddies have decayed only larger eddies remain and, since they are larger, their effective centres are farther from the wall and they move at a faster speed owing to the higher mean velocities farther from the wall.

Although the convection speeds in the plane and axially symmetric boundary layer are the same there are important differences between the space-time correlation for the two cases. In the boundary layer with transverse curvature, the rate of decay of the maximum of the space-time correlation is more rapid than it is in the plane boundary layer. Referring to figure 10, we see that when $x_1/\delta^* = 9{\cdot}33$ the maximum pressure correlation is $R_{pp} = 0{\cdot}1$. In the case of the plane boundary layer (Willmarth & Wooldridge 1962) $R_{pp} = 0{\cdot}1$ occurs for $x_1/\delta^* = 22{\cdot}6$. The decay of the maximum (or peak) value of the pressure correla-

† Or use numerous closely spaced transducers.

tions for plane and axially symmetric boundary layers are shown in figure 13, where $R_{pp}(x_1, 0, \tau_c)$ is the peak value of the pressure correlation. From the figure, it can be observed that in the boundary layer with transverse curvature, the decay of pressure correlation is more rapid than it is in a plane boundary layer. Additional measurements of convection speeds have been obtained from space-time correlation measurements with $x_3 \neq 0$. These are discussed in appendix B.

5.2. *Longitudinal, lateral and oblique spatial correlations of the wall pressure*

The spatial correlations of the wall pressure (with zero time delay) have been studied in considerable detail to determine the contours of constant pressure correlation on the surface of the cylinder. The array of thirteen pressure transducers (see figure 4), was designed so that a large number of pressure correlations for different spatial separations could be efficiently measured with a small number of pressure transducers. All of the wall-pressure correlations, at zero time delay, were measured in the frequency band $0{\cdot}144 < (\omega\delta^*/U_\infty) < 28{\cdot}8$, and have been corrected for effect of sound in the free stream (see appendix A).

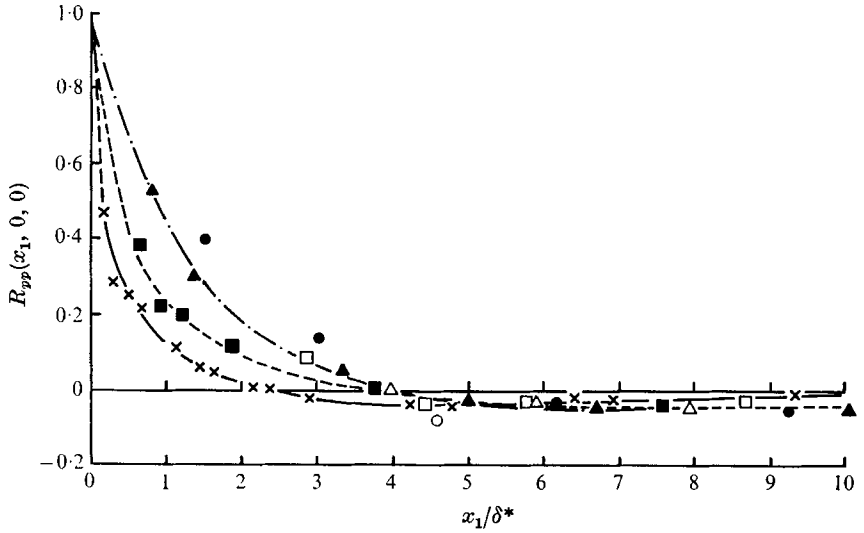

FIGURE 14. Longitudinal wall-pressure correlation in a broad frequency band. ×, $\delta/a = 2$, all others, $\delta/a = 0$. ■, $R_\theta = 38{,}000$, Willmarth & Wooldridge; ●, $R_\theta = 10{,}000$, Bull; ▲, $R_\theta = 19{,}500$, Bull; ○, $R_\theta = 11{,}000$, Bull; △, $R_\theta = 24{,}300$, Bull; □, $R_\theta = 33{,}800$, Bull.

The results of the spatial correlation measurements are displayed in figures 14 to 17. Consider figures 14 and 15 which show the longitudinal and lateral pressure correlation. It is clear that the pressure correlation decreases with x_1 or x_3 more rapidly than has been observed in the plane boundary layer. For the present case of a boundary layer with transverse curvature in which $\delta/a \approx 2$, the lateral or longitudinal spacing at which any given positive value of the pressure correlation is attained is the order of half or less than the spacing at which the same value of pressure correlation is attained in the plane boundary layer.

Figures 16 and 17 show measurements of spatial correlation in oblique directions, along a 45° line in figure 16 and for various oblique locations in figure 17.

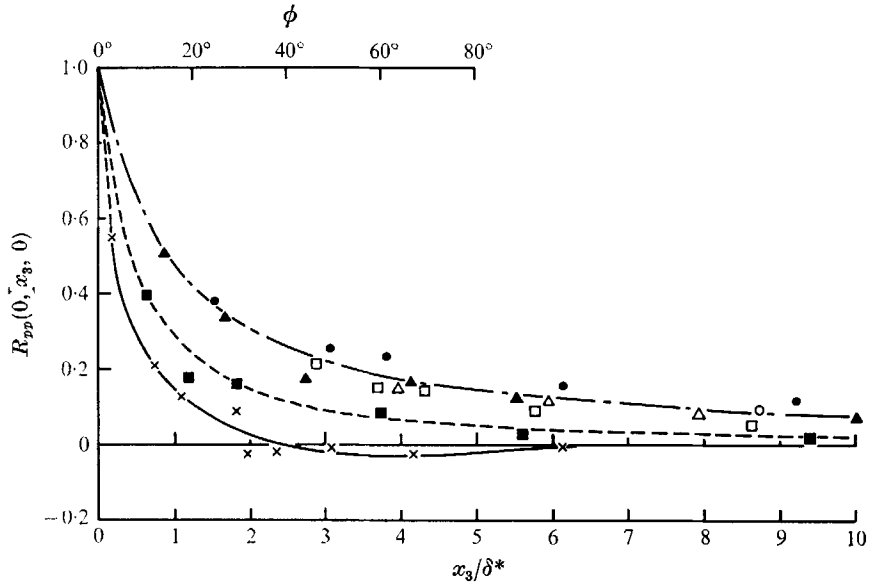

FIGURE 15. Transverse wall-pressure correlation in a broad frequency band. Same symbols as figure 14.

In these measurements, using the array of transducers of figure 4, we have assumed that the random wall-pressure field is statistically homogeneous. Thus, we ignore the rather slow streamwise changes in the statistical structure of the wall-pressure field.

The results of all the measurements of pressure correlation with zero time delay are summarized and compared with the plane boundary-layer case in figures 18 and 19, respectively.

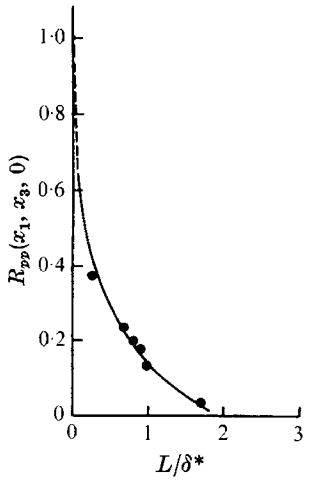

FIGURE 16. Spatial correlations of the wall pressure along a line at 45° to the flow direction. L is distance along the 45° line.

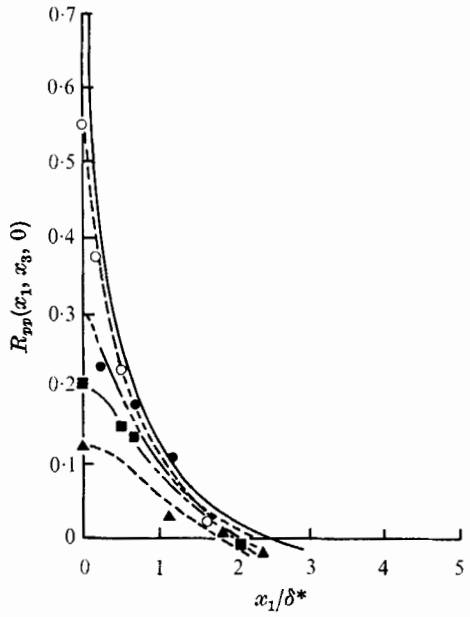

FIGURE 17. Spatial correlation of the wall pressure, additional measurements. ——, $x_3/\delta^* = 0$; --○--, $x_3/\delta^* = 0{\cdot}19$; --●--, $x_3/\delta^* = 0{\cdot}48$; --■--, $x_3/\delta^* = 0{\cdot}72$; --▲--, $x_3/\delta^* = 1{\cdot}10$.

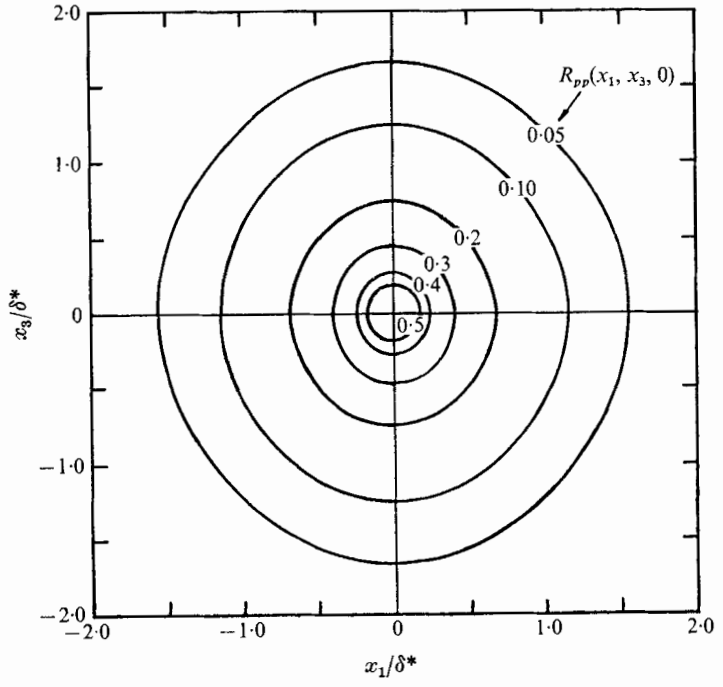

FIGURE 18. Contours of constant wall-pressure correlation.

Figure 18 shows that the contours of constant pressure correlation are very nearly circular and have decayed to 1/20 of the maximum value in a distance of approximately $1{\cdot}5\delta^*$. (Note that in this experiment $\delta^* = 0{\cdot}43$ in. and $\delta = 2{\cdot}8$ in.) In the lateral direction, a distance $x_3 = 1{\cdot}5\delta^*$ corresponds to only 23·7 degrees of arc along the cylinder.

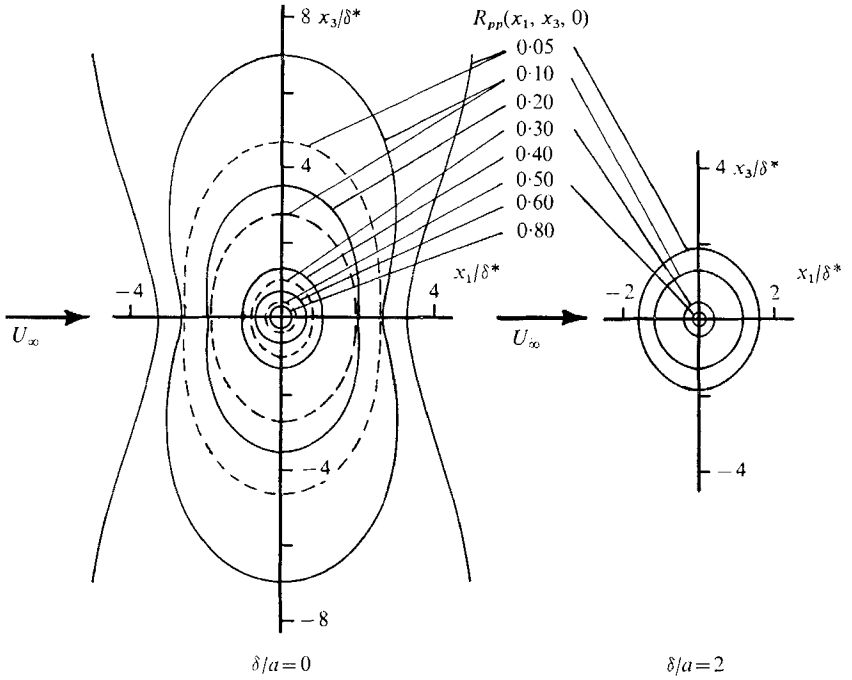

FIGURE 19. Effect of transverse curvature on contours of constant wall-pressure correlation. ——, Bull; – – – –, Willmarth & Wooldridge.

In figure 15, the lateral pressure correlation is negligibly small for $x_3/\delta^* \geqslant 6{\cdot}2$ and does not appear to oscillate. We do not believe that there would be a significant correlation of the wall pressure (relative to the value of $R_{pp} = 0{\cdot}05$ at $x_3/\delta^* = 1{\cdot}5$) for points on opposite sides of the cylinder. We have filtered out all pressure fluctuations with a frequency less than 100 Hz ($\omega\delta^*/U_\infty < 0{\cdot}144$) and, since the convection speed is of the order of $0{\cdot}8U_\infty$ the half wavelength of the pressure fluctuations that have been rejected is already quite large, of the order of 2·5 cylinder diameters. Recall that the pressure correlation of figures 14 and 15 is essentially zero in a much smaller distance, of the order of half the diameter of the cylinder.†

Figure 19 compares the contours of constant correlation for plane and axially symmetric boundary layers. The iso-correlation contours in the axially symmetric boundary layer are nearly circular as compared to the case of the plane boundary layer in which the larger iso-correlation contours, for smaller values of R_{pp},

† Difficulties caused by the vibration sensitivity of the pressure transducers and spatial limitations inside the cylinder made it impossible to measure the correlation between pressure on opposite sides of the cylinder.

are elongated in the transverse, x_3, direction. For large values of R_{pp} (small size iso-correlation contours) the shape of the iso-correlation contours is nearly circular for both the plane and axially symmetric boundary layer.

From these results it is apparent that the effect of transverse curvature is to reduce the scale of all the random pressure-producing eddies (by a factor of two or more for the present experiment with $\delta/a \approx 2$). The reduction in transverse scale of the larger eddies is greater than the longitudinal scale reduction. The scale reduction of the smaller eddies is approximately the same in the longitudinal and transverse directions.

5.3. *Power spectrum of the wall pressure*

The power spectrum of the wall-pressure fluctuations beneath the axially symmetric turbulent boundary layer at $U_\infty = 145$ ft./sec was measured in the frequency range from 100 to 20,000 Hz ($0{\cdot}144 \leqslant (\omega\delta^*/U_\infty) \leqslant 28{\cdot}8$) using the pressure transducers described in §3.2 with $R/\delta^* = 0{\cdot}072$. The data were compared with the power spectrum in the plane boundary layer measured with a pressure transducer with $R/\delta^* = 0{\cdot}061$ by Willmarth & Roos (1965) and with a pressure transducer with $R/\delta^* = 0{\cdot}095$ by Bull *et al.* (1963) (see figure 20). The reason for choosing 100 Hz as the lower frequency limit for the measurements was the possibility of free-stream temperature and vorticity disturbances caused by heat input or cooling at the wall of the wind tunnel circuit. A description of our observations of this phenomenon are given in Willmarth & Wooldridge (1962). However, in the present investigation, we did not observe the severe pressure disturbances at low frequencies that were found at the wall (Willmarth & Wooldridge 1962). The reason may be that the effects of external heat input or cooling remain confined to a region near the wind tunnel wall. Generally speaking, the shape of the wall-pressure spectra beneath a two-dimensional boundary layer and beneath a boundary layer with transverse curvature do not appear greatly different on a log-log plot. However, on closer examination one finds that at high frequencies, $\omega\delta^*/U_\infty > 10$, the wall-pressure spectrum beneath the boundary layer with transverse curvature contains approximately twice the energy density that was measured beneath a plane boundary layer and at low frequencies, $\omega\delta^*/U_\infty < 1$, the energy density of the pressure spectrum beneath the boundary layer with transverse curvature is 75 % less than beneath a plane boundary layer. The normalized power spectra are shown on a linear scale in figure 22. It is quite clear on the linear scale that there is, indeed, greater spectral density at high frequencies. The data of figure 22 have been corrected for the effects of attenuation caused by the finite size of the pressure transducer. This is discussed below.

5.4. *Corrections for finite transducer size*

Experimental resolution of the structure of the turbulent pressure field is limited by the finite size of the pressure transducer. For a transducer of diameter $2R$, the measurements of the spectrum of the pressure at a frequency of the order of $U_\infty/2R$ or greater will be subject to a considerable error which becomes larger as the frequency increases. Therefore, it is desirable to use as small a diameter transducer as possible. In the present investigation, the diameter of the trans-

ducer was 0·06 in. and the frequency $U_\infty/2R$ was 30KHz. (Note that most of the energy in the spectra of figure 20 occurs at frequencies less than 20KHz.) Therefore, the present results should not be subject to a large error.

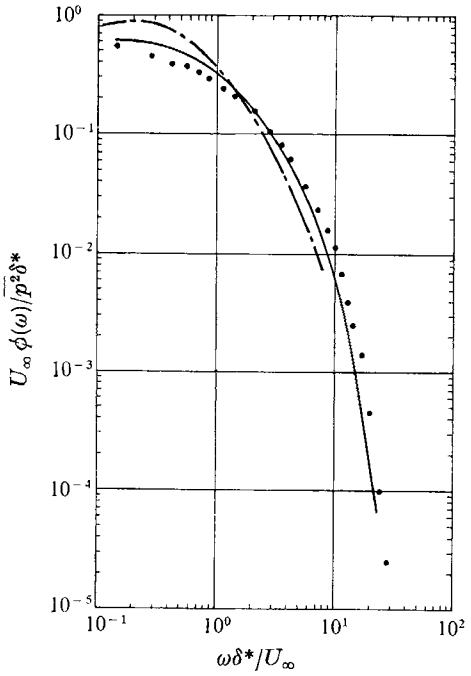

FIGURE 20. Measured wall-pressure spectra. ●, $\delta/a = 2$, $R/\delta^* = 0{\cdot}07$, $R_{\delta^*} = 32{,}100$; — — —, $\delta/a = 0$, $R/\delta^* = 0{\cdot}10$, $R_{\delta^*} = 25{,}400$, Bull; ——, $\delta/a = 0$, $R/\delta^* = 0{\cdot}06$, $R_{\delta^*} = 49{,}400$, Willmarth & Roos.

Corrections to the power spectrum measured by a finite size transducer beneath a plane boundary layer have been computed by Corcos (1963). His calculations assume that the pressure field can be represented as a function of the similarity variables $\omega x_1/U_c$ and $\omega x_3/U_c$. For this reason and others, related to the method of calculation, his corrections are an approximation to the true corrections. However, Corcos's corrections agree with our plane boundary layer experimental results and calculations (Willmarth & Roos 1965), when $\omega R/U_c < 1$.

We have used Corcos' (1963) computations for the correction of our power spectrum beneath the boundary layer with transverse curvature in the range of interest for our spectrum (for $\omega R/U_c < 1$). Note that using Corcos' computations means that the wall pressure must be expressible using the similarity variables and functions used by Corcos (1963). To a reasonable† approximation this is true and is discussed in appendix C. The corrected power spectrum nondimensionalized by r.m.s. wall pressure is presented on a logarithmic scale in

† The major difficulty is that the function $B(\omega x_3/U_c)$ is not unique (see figure 28). However, we expect that the corrections (which are not too large) will not be seriously in error.

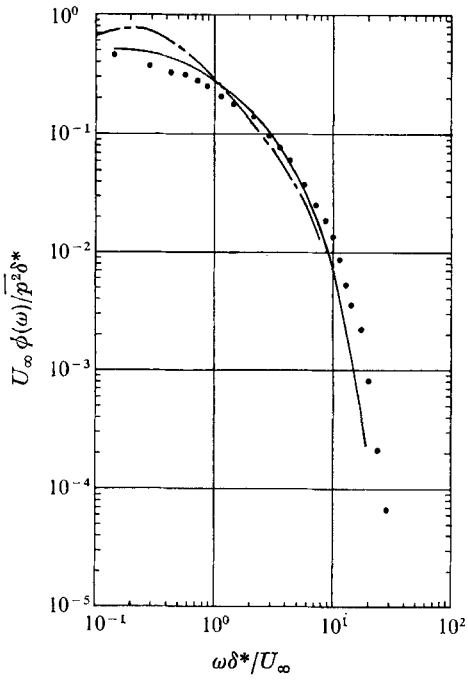

FIGURE 21. Wall-pressure spectra corrected for finite size transducer. Symbols same as figure 20.

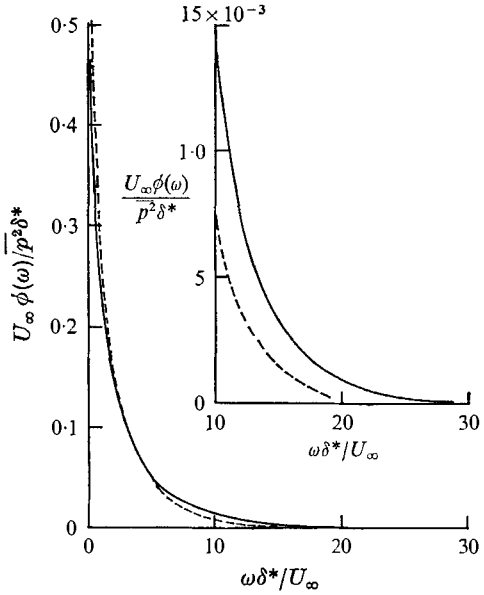

FIGURE 22. Wall-pressure spectra of figure 21 on linear scale. ——, $\delta/a = 2$; – – – –, $\delta/a = 0$, Willmarth & Roos.

figure 21 and on a linear scale in figure 22. For comparison, the corrected dimensionless power spectrum of the plane boundary-layer wall pressure measured by other investigators are also presented in the figures.

The corrected root-mean-square wall pressure is listed in table 3. Note that the correction to the root-mean-square wall pressure is small (of the order of 10 %). More accurate computations of the corrected root-mean-square wall pressure are probably not necessary.

5.5. *Root-mean-square wall pressure*

The root-mean-square (r.m.s.) value of the pressure fluctuations on the surface of a cylinder was measured in the frequency band $0{\cdot}063 < \omega\delta^*/U_\infty < 57{\cdot}6$. The measurements are compared with the r.m.s. wall pressure associated with plane boundary layer obtained by other investigators in table 3. All the data has been corrected for the presence of sound in the free stream and for the effect of finite transducer size as noted in table 3.

	$\sqrt{(\overline{p^2})}/q_\infty$	$\sqrt{(\overline{p^2})}/\tau_w$	R_θ	Frequency range		Remarks
Axially symmetric boundary layer	$5{\cdot}6 \times 10^{-3}$	2·39	26,200	$0{\cdot}063 < \omega\delta^*/U_\infty < 57{\cdot}6$	Uncorrected	Present data, $R/\delta^* = 0{\cdot}072$
	$5{\cdot}99 \times 10^{-3}$	2·56	26,200	$0{\cdot}063 < \omega\delta^*/U_\infty < 57{\cdot}6$	Corrected	
Plane boundary layer	$5{\cdot}14 \times 10^{-3}$	2·54	38,000	$0{\cdot}14 < \omega\delta^*/U_\infty < 28{\cdot}8$	Uncorrected	Willmarth & Roos (1965), $R/\delta^* = 0{\cdot}061$
	$5{\cdot}64 \times 10^{-3}$	2·66	38,000	$0{\cdot}14 < \omega\delta^*/U_\infty < 28{\cdot}8$	Corrected	
	$5{\cdot}35 \times 10^{-3}$	2·48	19,500	$0{\cdot}016 < \omega\delta^*/U_\infty < 19{\cdot}9$	Corrected	Bull *et al.* (1963)
	$5{\cdot}45 \times 10^{-3}$	2·58	26,000	$0{\cdot}087 < \omega\delta^*/U_\infty < 11$	Corrected	
	$5{\cdot}4 \times 10^{-3}$	2·80	33,800	$0{\cdot}14 < \omega\delta^*/U_\infty < 17$	Corrected	

TABLE 3. Comparison of root-mean-square values of the wall-pressure fluctuations

According to Bull *et al.* (1963), the ratio of r.m.s. wall pressure to free stream dynamic pressure is not dependent on Reynolds number. However, the ratio of r.m.s. wall pressure to skin friction increases slightly when Reynolds number increases because the skin friction coefficient decreases as Reynolds number increases. If we compare the ratios $\overline{p^2}/q_\infty$ or $\overline{p^2}/\tau_w$ for the plane and axially symmetric boundary layers (see table 3), we find that there is not a large change in either ratio caused by transverse curvature. For instance, the corrected ratio of r.m.s. wall pressure to dynamic pressure beneath an axially symmetric boundary layer is only 7 % larger than the value measured by Willmarth & Roos (1965) at slightly higher Reynolds number. Recalling that transverse curvature increases the mean skin friction, we note that $\sqrt{(\overline{p^2}/\tau_w)}$ is the same (at $R_\theta = 26{,}000$) as in a plane boundary layer. In any event, there is not a large effect of transverse curvature on the root-mean-square wall pressure for $\delta/a \leqslant 2$.

5.6. *Integral spatial and temporal scales*

The integral scales of the wall pressure were computed according to the formulae

$$\Lambda_1 = \int_{-\infty}^{\infty} |R_{pp}(x_1, 0, 0)|\, dx_1, \tag{19}$$

$$\Lambda_3 = \int_{-\infty}^{\infty} |R_{pp}(0, x_3, 0)|\, dx_3, \tag{20}$$

$$\Lambda_\tau = \int_{-\infty}^{\infty} |R_{pp}(0, 0, \tau)|\, d\tau, \tag{21}$$

where Λ_1, Λ_3 and Λ_τ are respectively the longitudinal, lateral and temporal integral scale. We have used the absolute value of pressure correlation in our definitions to ensure that spuriously small integral scales are not produced by oscillations of the pressure correlation caused by the rejection of low frequencies when the signals were filtered.

The various integral scales are collected for comparison with the case of a plane boundary layer in table 4. It is apparent that in all cases the effect of lateral transverse curvature is to reduce the spatial and temporal integral scales. It is clear and not too surprising that transverse curvature reduces the lateral integral scale, Λ_3, by a larger amount (a factor of 2·5 or more) than the reduction of the longitudinal and temporal scales (a factor of the order of 1·5).

	Axially symmetric boundary layer	Plane boundary layer	
Frequency range	$0{\cdot}144 < \frac{\omega\delta^*}{U_\infty} < 28{\cdot}8$	$0{\cdot}14 < \frac{\omega\delta^*}{U_\infty} < 13{\cdot}6$	$0{\cdot}075 < \frac{\omega\delta^*}{U_\infty} < 7{\cdot}5$
$\Lambda_\tau U_\infty/\delta^*$	2·92	3·90	3·84
Λ_1/δ^*	1·31	2·06	3·20
Λ_3/δ^*	1·04	2·51	6·74
Remarks		Willmarth & Wooldridge (1962)	Bull *et al.* (1963)

TABLE 4. Integral spatial and temporal scales in plane and axially symmetric turbulent boundary layers

6. Summary and discussion

From the results of our measurements presented in § 5, we can make a qualitative assessment of the effect of transverse curvature on the structure of turbulence and on the wall pressure.

First consider the result of figures 11 and 12 which show that the convection speed in the boundary layer with transverse curvature is almost the same as in a plane boundary layer. Next, consider the velocity profiles in the plane and axially symmetric boundary layers which are compared in figure 23 where the displacement thickness, δ^*, has been used as a length scale. We have used δ^* exclusively for our length scale in presenting our results because it is a more definite quantity than δ and has been successfully used in the case of the plane boundary layer. (As a matter of fact, our qualitative discussion would not be changed if θ or δ were used as the characteristic length.) From figure 23, it is apparent that the velocity profile is much 'fuller' when transverse curvature is present. Consider a turbulent pressure producing eddy in contact with the wall of any given size (relative to δ^*). It is clear that if an eddy of this given size is present in a boundary

layer with transverse curvature, it will have a higher convection velocity than it would have in a plane boundary layer (because at every point in the eddy the mean velocity would be larger). On the other hand, as mentioned above, the measured convection velocity in the two boundary layers is nearly the same. The explanation for the unchanged convection velocity is that the pressure-producing eddies in the boundary layer with transverse curvature must be smaller and therefore nearer the wall where the mean velocity is lower.

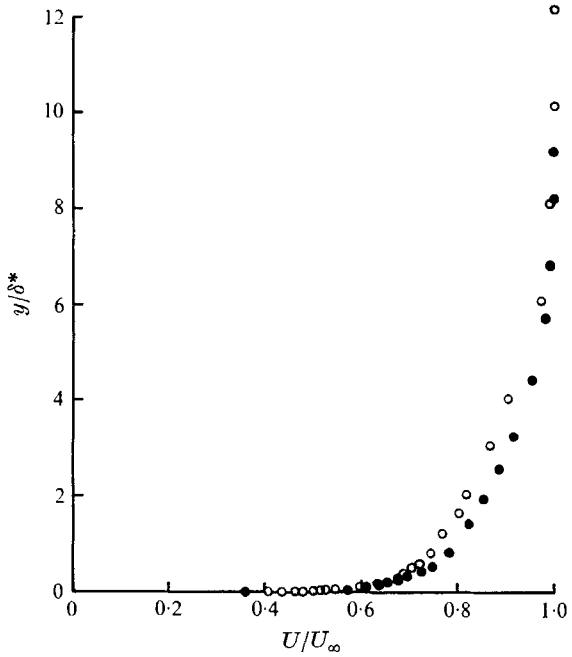

FIGURE 23. Comparison of the mean velocity profiles. ●, $\delta/a = 2$, $R_\theta = 26{,}200$; ○, $\delta/a = 0$, $R_\theta = 38{,}000$, Willmarth & Wooldridge.

The assertion that the pressure-producing eddies are smaller (relative to δ^*) in a boundary layer with transverse curvature is in agreement with all our other measurements.

Consider the relative size of the contours of constant pressure correlation of figure 19. In a boundary layer with transverse curvature, the contours are smaller by approximately a factor of two or more than they are in a plane boundary layer. Figure 13 shows the decay of the peaks of longitudinal space-time correlation. The decay is much more rapid at small spatial separation in a boundary layer with transverse curvature† and this is caused by the presence of smaller eddies that are created by the transverse curvature. (Recall that Willmarth & Wooldridge (1962) have shown that an eddy of any given size decays after

† Note that in figure 13 for $x_1/\delta^* > 6$ the rate of decay of the maxima of the pressure correlation in the plane and axially symmetric boundary layer is the same. This indicates that after the smaller eddies have decayed, the eddy size distribution of larger eddies is similar in the boundary layer on a plane and cylindrical surface.

travelling a distance proportional to its size.) Thus, if there are relatively more smaller eddies, the pressure correlation will decay in a shorter distance. Finally, the power spectrum of the wall pressure (see figure 22) contains a greater energy density at high frequencies than in a plane boundary layer owing to the unchanged convection speed of smaller eddies.

Consider the contours of constant pressure correlation of figure 18 which are compared with those beneath a plane boundary layer in figure 19. In general, the constant pressure correlation contours are nearly circular and smaller in size than those beneath a plane boundary layer. Note that beneath a plane boundary layer the larger contours of constant pressure correlation ($R_{pp} \leqslant 0{\cdot}1$) are elongated transverse to the stream while the smaller contours ($R_{pp} > 0{\cdot}3$) are nearly circular.

We suggest that there are two primary effects in a boundary layer with transverse curvature that reduce the size of turbulent eddies (and the correlation contours). The first effect which causes a reduction in size of the eddies is the increased fullness of the velocity profile.† In a boundary layer with a fuller velocity profile the turbulent eddies near the wall moving at any given convection speed must be smaller because the mean velocity corresponding to that convection speed is reached at a point nearer the wall. In addition, there is a second (more direct) effect in which the large eddies suffer a greater reduction in transverse scale than small eddies because the wall is curved transversely. Thus, if one visualizes a large eddy adjacent to the curved wall, it is apparent that in the transverse direction at either side of the periphery of a large eddy the mean velocity is higher than it would be at the sides of the same eddy in a plane boundary layer. There is a streamwise shearing motion along the sides of large eddies in a boundary layer with transverse curvature that is not present in a plane boundary layer. This shearing motion also acts to reduce the transverse scale of large eddies.‡

Additional confirmation for the selective effect of transverse curvature on the lateral scale of large pressure producing eddies is contained in appendix C. There, the effect of transverse curvature on the spatial decay of the narrow band correlation of the pressure in a lateral direction is more rapid for large eddies (in a low-frequency band) than it is for small eddies (in a high-frequency band).

We are grateful to Hugh Fitzpatrick for suggesting that these measurements be made. The research was supported by the Fluid Dynamics Branch of the Office of Naval Research.

Appendix A. Correction of wall pressure for the effect of sound in the free stream

The pressure measured at the wall is

$$p_m = p + p_s, \tag{A 1}$$

† See the discussion of §1, about the effect of transverse curvature on the mean velocity profile.

‡ If we consider the extreme case of large transverse curvature with $\delta/a \to \infty$, the transverse extent of the largest eddy is limited to a distance of the order of 2δ. For a plane boundary layer there is no readily apparent limiting transverse length.

where p is the turbulent wall pressure and p_s is the pressure produced by sound waves in the free stream. We assume the wavelength of sound is large compared to the maximum, 0·33 ft., separation distance between points where p_1 and p_2 are measured. The correction is valid for sound of wavelength larger than, say, 3 ft. or for frequencies lower than 400 Hz. The sound field in the tunnel contains large peaks at frequencies less than 200 Hz (Willmarth & Wooldridge 1962). The correction is sufficiently accurate for our data. The measured pressure correlation is

$$(R_{pp})_m = \frac{\overline{(p_1+p_s)(p_2+p_s)}}{\overline{(p+p_s)^2}} = \frac{(R_{pp})_t + \overline{p_s^2}/\overline{p^2}}{1+\overline{p_s^2}/\overline{p^2}}, \tag{A 2}$$

where we assume $\overline{p_1^2} = \overline{p_2^2}$, $\overline{p_1 p_s} = \overline{p_2 p_s} = 0$, and the true pressure correlation is $(R_{pp})_t = \overline{p_1 p_2}/\overline{p^2}$. Therefore

$$(R_{pp})_t = (1+\overline{p_s^2}/\overline{p^2})(R_{pp})_m - \overline{p_s^2}/\overline{p^2}. \tag{A 3}$$

For Willmarth & Wooldridge's (1962) data $\overline{p_s^2}/\overline{p^2} = 0{\cdot}05$ and for the present data $\overline{p_s^2}/\overline{p^2} = 0{\cdot}02$.

Appendix B. Convection speeds measured in oblique directions

From the results of oblique ($x_3 \neq 0$) space-time correlation measurements, the locus of the peaks of pressure correlation were plotted in figure 24 as a function of longitudinal spatial separation for several obliquities (various values of x_3/δ^*). Figure 24 shows that the location of the peaks of the pressure correlation in the x_1, τ plane remains the same as it was for $x_3 = 0$. Thus, the decay of the wall pressure in the transverse direction does not directly effect the convection speed in the longitudinal direction.

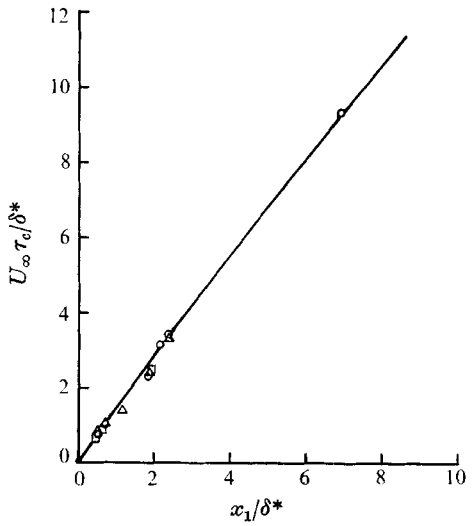

FIGURE 24. Time delay for R_{pp} maximum at various constant values of x_1 and x_3. ——, $x_3/\delta^* = 0$ (see figure 11); ○, $x_3/\delta^* = 0{\cdot}48$; □, $x_3/\delta^* = 0{\cdot}72$; △, $x_3/\delta^* = 1{\cdot}10$.

Appendix C. Correlation of the wall pressure in narrow-frequency bands

Let $p(x, z, t; \omega)$ be the signal obtained by passing the output of a pressure transducer at (x, z) through an ideal filter which has a narrow pass band centred at a frequency, ω, whose width is $\Delta\omega$. Then the correlation of pressure fluctuations measured by two pressure transducers a distance (x_1, x_3) apart at central frequency ω for a band width $\Delta\omega$ is

$$Q'_{pp}(x_p, x_3, \tau; \omega) = (1/T)\int_0^T p(x, z, t, \omega)\, p(x + x_1, z + x_3, t + \tau; \omega)\, dt. \quad \text{(C 1)}$$

The narrow band correlation coefficient is defined as

$$R'_{pp}(x_1, x_3, \tau; \omega) = \frac{Q'_{pp}(x_1, x_3, \tau; \omega)}{Q'_{pp}(0, 0, 0; \omega)}. \quad \text{(C 2)}$$

Corcos (1962) suggested that R'_{pp} could be represented by the expression†

$$R'_{pp}(x_1, x_3, \tau; \omega) = A\left(\frac{\omega x_1}{U_c}\right) B\left(\frac{\omega x_3}{U_c}\right) \cos\left(\omega\tau - \frac{\omega x_1}{U_c}\right). \quad \text{(C 3)}$$

Relatively narrow-band correlations of the wall pressure were measured in the four frequency bands

$$\left.\begin{aligned} 0{\cdot}61 &< \frac{\omega\delta^*}{U_\infty} < 0{\cdot}97 \\ 1{\cdot}28 &< \frac{\omega\delta^*}{U_\infty} < 2{\cdot}76 \\ 3{\cdot}87 &< \frac{\omega\delta^*}{U_\infty} < 6{\cdot}25 \\ 5{\cdot}21 &< \frac{\omega\delta^*}{U_\infty} < 15{\cdot}63 \end{aligned}\right\} \text{Central frequency at } \frac{\omega\delta^*}{U_\infty} \left\{\begin{aligned} &0{\cdot}79 \\ &2{\cdot}02 \\ &5{\cdot}06 \\ &10{\cdot}42. \end{aligned}\right.$$

To carry out these measurements two Krohn-Hite model 310-AB variable band-pass filters were used. The high and low pass settings of the two filters were carefully matched to give nearly identical phase shift as a function of frequency (within $\pm 3°$).

From the measured space-time correlation curves, values of correlation amplitude and convection speed were obtained. Figure 25 shows the convection speed for increasing values of spatial separation in various frequency bands. The convection speed of figure 25 is obtained in the same way as that described in §5.1. Figure 25 shows an increase in convection speed as the longitudinal spatial separation increased. Part of the increase is caused by the finite band width of the filter since the smaller eddies in the finite band width decay faster than the larger ones (see §5.1). The asymptotic values of convection speed at large spatial separation were plotted in figure 26 as a function of dimensionless frequency $\omega\delta^*/U_\infty$. Comparing figure 26 with Willmarth & Wooldridge's (1962) data shows that the asymptotic convection speed (i.e. $x_1/\delta^* \to \infty$) of a given size eddy in the axially symmetric boundary layer is almost identical to that obtained in the plane boundary layer.

† See Bull (1961) for a complete discussion.

The amplitude function $A(\omega x_1/U_c)$ of the narrow-band longitudinal correlation of Corcos' representation can be found by plotting the measured maximum amplitude of space-time correlation, i.e. $R_{pp}(x_1, 0, \tau_c, \omega)$, for various spatial separations and central frequencies (figure 27). The amplitude of narrow-band longitudinal space-time correlation is only slightly less than in the plane boundary layer. This means that in the stream direction the rate of decay of a given size eddy is about the same as in the plane boundary layer and the rate of decay is proportional to the size of the eddy.

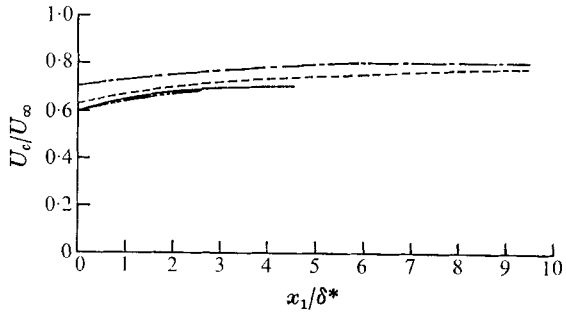

FIGURE 25. Local convection speed of pressure-producing turbulent eddies in various frequency bands. ———, $\omega\delta^*/U_\infty = 0{\cdot}79$; – – – –, $\omega\delta^*/U_\infty = 2{\cdot}02$; ——, $\omega\delta^*/U_\infty = 5{\cdot}06$; ——– – –, $\omega\delta^*/U_\infty = 10{\cdot}42$.

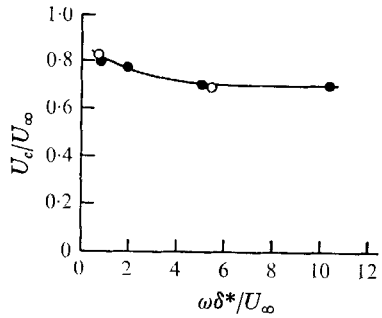

FIGURE 26. Asymptotic convection speed as a function of frequency. ●, $\delta/a = 2$; ○, $\delta/a = 0$, Willmarth & Wooldridge.

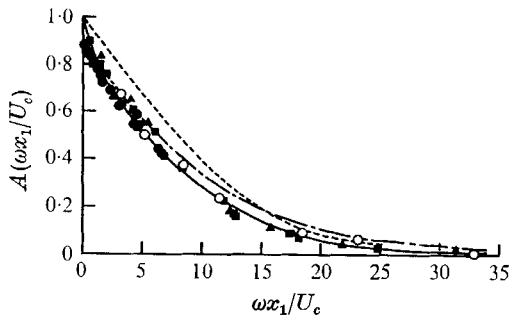

FIGURE 27. Amplitude of narrow-band longitudinal space-time correlation of the wall pressure, $x_3 = 0$. —●—, $\delta/a = 2$, $\omega\delta^*/U_\infty = 0{\cdot}79$; —■—, $\delta/a = 2$, $\omega\delta^*/U_\infty = 2{\cdot}02$; —▲—, $\delta/a = 2$, $\omega\delta^*/U_\infty = 5{\cdot}06$; —○—, $\delta/a = 2$, $\omega\delta^*/U_\infty = 10{\cdot}42$; – – – –, $\delta/a = 0$, Bull; ——– – –, $\delta/a = 0$, Willmarth & Wooldridge.

The amplitude of transverse correlation in Corcos's representation $B(\omega x_3/U_\infty)$, was obtained by plotting the measured transverse correlations at zero time delay as a function of $\omega x_3/U_\infty$,† (see figure 28). The measurements show that the amplitude of narrow-band transverse correlation for $x_3/\delta^* = 0{\cdot}191$ is nearly the same as in a plane boundary layer. But for $x_3/\delta^* \geqslant 0{\cdot}722$, the transverse correlations fall off much more rapidly than they do in a plane boundary layer as $\omega x_3/U_\infty$ increases.

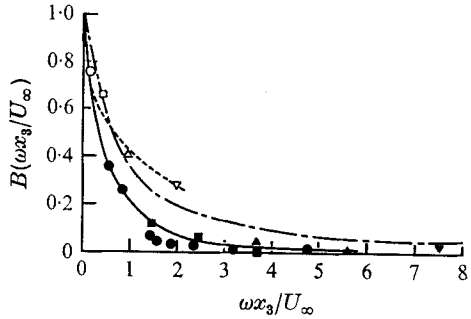

FIGURE 28. Amplitude of narrow-band transverse space-time correlation of the wall-pressure. For the cases $x_3/\delta^* = 0{\cdot}19$, $\delta/a = 2$: --○--, $\omega\delta^*/U_\infty = 0{\cdot}79$; --□--, $\omega\delta^*/U_\infty = 2{\cdot}02$; --△--, $\omega\delta^*/U_\infty = 5{\cdot}06$; --▽--, $\omega\delta^*/U_\infty = 10{\cdot}42$. For the cases $x_3/\delta^* \geqslant 0{\cdot}72$, $\delta/a = 2$: —●—, $\omega\delta^*/U_\infty = 0{\cdot}79$; —■—, $\omega\delta^*/U_\infty = 2{\cdot}02$; —▲—, $\omega\delta^*/U_\infty = 5{\cdot}06$; —▼—, $\omega\delta^*/U_\infty = 10{\cdot}42$. For $\delta/a = 0$: – – –, Willmarth & Wooldridge.

The approximate relation (equation (C3)), suggested by Corcos, appears to be reasonably accurate if $x_3 = 0$ (see figure 27). However, if $x_1 = 0$ and $x_3 \neq 0$, the function $B(\omega x_3/U_c)$ is not unique (see figure 28). This is apparently an effect caused by transverse curvature since a single function $B(\omega x_3/U_c)$ suffices for a plane boundary layer. Actually, the formulation of (C 3) is only an approximation even for the plane boundary layer and does break down in that case also; see Bull *et al.* (1963) who showed that for very low frequencies $A(\omega x_1/U_c)$ and $B(\omega x_3/U_c)$ were not unique.

REFERENCES

ALEXANDER, L. G., BARON, T. & COMINGS, E. W. 1953 *University of Illinois Engineering Experiment Station, Bulletin*, Series no. 413.

BULL, M. K. 1961 *University of Southampton Report*, A.A.S.U. no. 200.

BULL, M. K., WILBY, J. F. & BLACKMAN, D. R. 1963 *University of Southampton Report*, A.A.S.U. no. 243; also 1967 *J. Fluid Mech.* **28**, 719.

CLAUSER, F. H. 1956 *Advances in Applied Mechanics*, vol. 4. New York: Academic Press.

COLES, D. 1954 *Z.A.M.P.* **5**, 181.

COLES, D. 1955 *50 Jahre Grenzshichtforschung* (ed. by Görtler and Tollmien). Braunschweig: F. Vieweg.

CORCOS, G. M. 1962 *University of California, Institute of Engineering Research, Report*, Series no. 183, Issue no. 2; also 1964 *J. Fluid Mech.* **16**, 353.

CORCOS, G. M. 1963 *J. acoust. Soc. Am.* **35**, 192.

† We have used the variable $\omega x_3/U_\infty$ instead of $\omega x_3/U_c$ because the function $B(\omega x_3/U_c)$ of Corcos (equation (C3)) was not unique.

GLAUERT, M. B. & LIGHTHILL, M. J. 1955 *Proc. Roy. Soc.* A **230**, 188.

MCMILLIAN, F. A. 1954 *J. Roy. Aeron. Soc.* **58**, 837.

MOORE, F. K. 1952 *N.A.C.A. Tech. Note*, no. 2722.

PATEL, V. C. 1965 *J. Fluid Mech.* **23**, 185.

PRESTON, J. H. 1954 *J. Roy. Aeron. Soc.* **58**, 109.

RAO, G. N. V. 1967 *J. appl. Mech. Trans. ASME*, **34**, 237.

REID, R. O. & WILSON, W. 1963 *J. Hydraulic Division, Proc. ASCE*, **89**, 21.

RICHMOND, R. L. 1957 *Guggenheim Aeronautical Laboratory, California Institute of Technology, Hypersonic Research Project Memo*, no. 39, and Thesis, California Institute of Technology.

SCHLICHTING, H. 1968 *Boundary Layer Theory*, 6th ed. New York: McGraw-Hill.

TU, B. J. & WILLMARTH, W. W. 1966 *University of Michigan, Tech. Rep.* 02920-3-T.

WILLMARTH, W. W. 1958*a* *J. Aeron. Sci.* **25**, 335.

WILLMARTH, W. W. 1958*b* *Rev. Scient. Instrum.* **29**, 218.

WILLMARTH, W. W. & ROOS, F. W. 1965 *J. Fluid Mech.* **22**, 81.

WILLMARTH, W. W. & WOOLDRIDGE, C. E. 1962 *J. Fluid Mech.* **14**, 187.

WILLS, J. A. B. 1964 *J. Fluid Mech.* **20**, 417.

YASUHARA, M. 1959 *Trans. Jap. Soc. Aero. Sci.* **2**, 72.

YU, Y. S. 1958 *J. Ship Res.* **2**, no. 3, 33.